Wireless Power Transfer

ARTICLE

Open Access

https://doi.org/10.48130/wpt-0025-0026

Wireless Power Transfer **2025**, 12: e022

Optimal frequency estimation for wireless power transfer systems with an active rectifier

Zhigang Zhang[1], Xiaodong Qing[1,2], Yanbao Liu[1], Tingfa Yang[1,3], Danli Chen[4], Fengwei Chen[4] and Zhao Chen[1,3*]

[1] *China Coal Technology and Engineering Group Chongqing Research Institute, Chongqing 400039, China*
[2] *Chongqing University of Science and Technology, Chongqing 401331, China*
[3] *Chongqing Anbiao Testing and Research Institute Co. Ltd, Chongqing 400052, China*
[4] *School of Automation, Chongqing University, Chongqing 400044, China*
* Corresponding author, E-mail: cz522376@139.com

Abstract

Wireless power transfer (WPT) technology, renowned for its reliability and flexibility, is utilized in numerous fields. This article addresses the synchronization of the active rectifier in WPT systems. Traditional methods for synchronization, such as auxiliary coil-based techniques, current sampling approaches, and perturbation observation methods, often suffer from limitations such as communication delays and sensitivity to noise. Meanwhile, they also assume the switch frequency is known. To overcome these flaws, this article proposes a frequency estimation method based on the sampled values of the rectifier bridge's input current. The method accurately estimates the frequency and initial phase angle, thus improving the synchronization performance. Additionally, dynamic clock interpolation technology is introduced to improve synchronization accuracy by compensating for quantization errors in pulse width modulation frequency generation. Simulation and experimental results demonstrate that the proposed method enhances both synchronization performance and stability, even if the realistic frequency is unknown.

Citation: Zhang Z, Qing X, Liu Y, Yang T, Chen D, et al. 2025. Optimal frequency estimation for wireless power transfer systems with an active rectifier. *Wireless Power Transfer* 12: e022 https://doi.org/10.48130/wpt-0025-0026

Introduction

With the advancement of technology, wireless power transfer (WPT) has garnered significant attention from academic and industrial communities due to its remarkable reliability and flexibility. The advantages of WPT have enabled its extensive application across various fields, notably including electric vehicles, oil exploration, biomedical engineering, aerospace, and marine engineering[1–7]. For WPT systems, the existing control methods can be categorized into two main types: primary-side control and secondary-side control. Primary-side control requires the reception of load information from the secondary side through a wireless communication module. However, wireless communication inevitably introduces an issue of communication delay, which affects the system's response speed and even causes instability[8]. Secondary-side control can avoid the drawback of primary-side control, but it requires the synchronization of the phases of the input voltage and current of the active rectifier. This is a challenging problem, especially when there is a discrepancy between the clock periods of the primary and secondary side controllers[9,10]. This necessitates further investigation into mitigating such issues. Several typical methods for achieving phase synchronization between the primary and secondary sides can be summarized as follows.

A synchronization technique is proposed for bidirectional WPT systems that employs an auxiliary winding to sense the magnetic field generated by the primary current, and utilizes a compensation winding to cancel out the effect of the pickup current, thereby producing an accurate synchronization signal that is used to synchronize the voltages of the primary and secondary converters[11]. The active single-phase rectifier (ASPR) with an auxiliary coil achieves synchronization based on zero-crossing detection. The current sensor is used to detect the current waveform of the rectifier input current, and then processes it through the band-pass filter and phase shift circuit to correct any phase error caused by the detection circuit[12]. However, the accuracy of synchronization depends on the design of the signal processing circuit and is very sensitive to system parameters. Auxiliary driving coils are added on the primary side to achieve phase synchronization between the primary and secondary sides without directly affecting the power transmission process[13,14]. By controlling the phase difference of these windings, the system can adjust the phase relationship between the primary and secondary power windings, but this leads to increased system complexity and cost[15].

Based on the detection and sampling of the ac current at the secondary side, synchronization can be achieved without an auxiliary coil. Synchronization is achieved through a controlled approach that relies on the measurement of both active and reactive power[16,17]. These techniques leverage the real and reactive power generated by the rectifier to either directly achieve synchronization or estimate the phase of the primary voltage, enabling the secondary side to synchronize with the primary side. However, both approaches rely on accurate power calculation and control. By detecting the zero crossing of the secondary resonant current or voltage, the synchronization signal[18–21] is triggered, and the phase difference is locked to achieve real-time frequency tracking, thereby avoiding the time-delay issues associated with wireless communication. However, the synchronization method based on detecting rectifier input current is sensitive to noise and harmonic interference, and requires complex filtering and algorithms, which limits its application in high-precision or fast tracking scenarios[22].

To overcome the shortcomings of the above synchronization methods, a strategy based on perturbation and observation is proposed[23,24]. The controller detects the input power, load voltage, and current from the power amplifier, and dynamically adjusts the equivalent load resistance of the rectifier. The latest research adopts perturbation and observation technology to track the extreme

value of the output current[25], achieve phase synchronization, and decouple the relative phase shift angle from the internal phase shift angle, thereby ensuring synchronization during the power regulation process. However, the primary and secondary sides always have different clock frequencies, which may cause failures in synchronization[13].

In existing methods, it is often assumed that the frequency of the pulse width modulation (PWM) module is known, and then the initial phase angle is estimated as the basis for synchronization. In case of a primary and secondary frequency mismatch, the initial becomes time varying, and the rate of variation will be proportional to the frequency error, significantly reducing the synchronization performance. To avoid this problem, a new method is proposed, which estimates simultaneously the frequency and initial phase angle of the rectifier input current, so as to reduce the demand for real-time performance of the synchronization algorithm.

The main contributions of this article are as follows: a method is proposed to simultaneously estimate the frequency and initial phase based on the sampling data of the rectifier input current. When the frequency is accurately estimated, the synchronization angle becomes constant, which greatly improves the accuracy of synchronization. These improvements not only improve the synchronization performance of the system but also reduce the requirements for the real-time processing ability of the algorithm, providing a new perspective and technical means for further research in related fields.

Problem statement

System description

This article report on series-series (SS), and dual-side LCC WPT systems. The dual-side LCC WPT system is investigated in this and the simulation verification sections, while the SS WPT system will be investigated in the experimental verification section. The circuit topology of the dual-side LCC WPT system is depicted in Fig. 1. Here, V_{dc} denotes the dc input voltage. The primary and secondary coils, L_p and L_s, are connected in series with their compensation capacitors C_p and C_s to compensate for the leakage inductance. Additionally, L_{f1} and C_{f1} represent the primary-side compensation inductance and capacitance, while L_{f2} and C_{f2} correspond to the secondary-side compensation inductance and capacitance. The output filter capacitor is denoted as C_f.

To simplify the analysis, the equivalent series resistances of the resonant components are neglected. The resulting simplified equivalent circuit is presented in Fig. 2. In this diagram, v_1 represents the output voltage of is inverter, i_1 denotes the output current of the inverter, i_p is the current flowing through the transmitting coil L_p, i_s is the current in the receiving coil L_s, and i_{f2} corresponds to the current fed to the rectifier.

The fundamental approximation is assumed in the following analysis. The phasor of v_1 is denoted as:

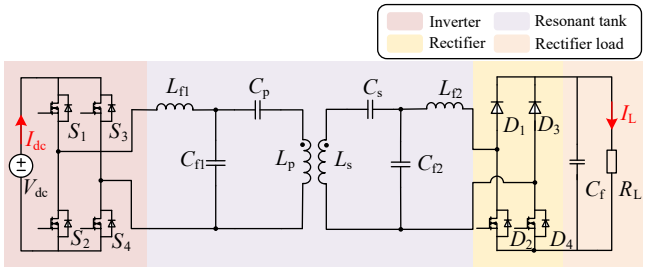

Fig. 1 Dual-side LCC WPT system with an active rectifier.

$$\dot{V}_1 = \frac{2\sqrt{2}V_{dc}}{\pi}\angle 0^\circ \tag{1}$$

while the equivalent resistance of the rectifier load with zero phase shift is approximated as:

$$R_{eq} = \frac{8}{\pi^2}R_L \tag{2}$$

The input impedance Z_{in}, secondary impedance Z_s, and reflected impedance Z_r are, respectively, expressed as follows:

$$\begin{aligned} Z_{in} &= j\omega L_{f1} + \left(j\omega L_p + \frac{1}{j\omega C_p} + Z_r\right) // \frac{1}{j\omega C_{f1}} \\ Z_s &= j\omega L_s + \frac{1}{j\omega C_s} + \frac{1}{j\omega C_{f2}} // (j\omega L_{f2} + R_L) \\ Z_r &= \frac{(\omega M)^2}{Z_s} \end{aligned} \tag{3}$$

and mutual inductance M is expressed as:

$$M = k\sqrt{L_p L_s} \tag{4}$$

The resonance conditions of the system are:

$$L_{f1}C_{f1} = L_{f2}C_{f2} = (L_p - L_{f1})C_p = (L_s - L_{f2})C_s \tag{5}$$

Substituting Eq. (5) into Eq. (3), it can be shown that:

$$Z_{in} = \frac{\omega^2 L_{f1}^2 L_{f2}^2}{M^2 R_L},\ Z_s = \frac{L_{f2}}{C_{f2}R_L} \tag{6}$$

The currents in the system have the following expressions:

$$\begin{aligned} \dot{I}_1 &= \dot{V}_1 \cdot \frac{M^2 R_L}{\omega_0^2 L_{f1}^2 L_{f2}^2}\angle 0^\circ \\ \dot{I}_p &= \dot{V}_1 \cdot \frac{1}{\omega L_{f1}}\angle -90^\circ \\ \dot{I}_s &= \dot{V}_1 \cdot \frac{MC_{f2}R_L}{L_{f1}L_{f2}}\angle 0^\circ \\ \dot{I}_2 &= \dot{V}_1 \cdot \frac{M}{\omega L_{f1}L_{f2}}\angle -90^\circ \end{aligned} \tag{7}$$

The output power under resonance is:

$$P_{out} = R_{eq} \cdot I_{f2}^2 \tag{8}$$

Through the above analysis, it is found that the dual-side LCC resonant compensation network has the following characteristics: When the system works in the resonant state, the impedance of the primary and secondary circuits is pure resistive, so the output voltage and current of the full bridge inverter on the primary side are in phase. The resonant inductor L_{f2} on the secondary side has a constant current independent of the load. Therefore, the dual-side LCC WPT system has a constant current output, and it is easy to achieve constant current control. In the rectifier bridge of this topology, a semi-active rectification approach is adopted, where D_1 and D_3 are diodes, and the driving signals for D_2 and D_4 are shown in Fig. 3.

Frequency mismatch problem

In practical applications, due to manufacturing tolerances in crystal oscillators and other factors, the secondary controller of a system often fails to generate a frequency identical to that of the primary controller. When there is a frequency mismatch between the

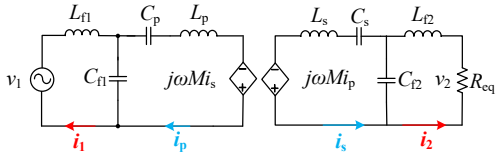

Fig. 2 Equivalent circuit of the dual-side LCC WPT system.

primary and secondary sides, this frequency difference can lead to inaccuracies in the estimation of the initial phase angle of the rectifier input current. This may affect the synchronization between the primary and secondary sides. In addition, this may cause fluctuations in the output dc voltage and current. Such issues pose significant challenges to the stability and control accuracy of the system, necessitating appropriate compensation or correction to mitigate the effects of frequency mismatch.

This is because when the primary and secondary side frequencies are inconsistent, if the actual frequency of the secondary controller is ω_s and the frequency of the primary controller is $\omega_s + \Delta\omega$, the estimated real-time phase of the rectifier input current should be:

$$\psi = (\omega_s + \Delta\omega)t + b = \omega_s t + (\Delta\omega t + b) \tag{9}$$

The PQ method is a technique based on the calculation of active power (P) and reactive power (Q) to estimate the phase angle between voltage and current. By leveraging these power components, the method enables accurate phase estimation. Specifically, for the rectifier input current $i_2 = a\sin(\omega t + b)$, the signal i_2 is decomposed into two orthogonal components through multiplication with $\cos(\omega t)$ and $\sin(\omega t)$. This process is illustrated in Fig. 4, where:

$$\begin{aligned} i_{p'} &= i_2\cos(\omega t) = \frac{a}{2}[\sin(b) + \sin(2\omega t + b)] \\ i_{q'} &= i_2\sin(\omega t) = \frac{a}{2}[\cos(b) - \cos(2\omega t + b)] \end{aligned} \tag{10}$$

It is evident that any signal can be regarded as the superposition of a dc component and an ac component. After being processed by a low-pass filter, the ac component is effectively attenuated, leaving only the dc component:

$$i_p = \frac{a}{2}\sin(b),\ i_q = \frac{a}{2}\cos(b) \tag{11}$$

from which the amplitude a and initial phase b can be computed as:

$$\begin{aligned} \hat{a} &= 2\sqrt{i_p^2 + i_q^2} \\ \hat{b} &= \begin{cases} \arctan\left(i_p/i_q\right), & i_q > 0, \\ \arctan\left(i_p/i_q\right) + \pi, & i_q < 0. \end{cases} \end{aligned} \tag{12}$$

In this process, a low-pass filter is used to remove high-frequency noise and high-order harmonics, so as to improve the accuracy of phase angle estimation. However, the time constant of the low-pass filter directly affects its rate of tracking a time-varying initial phase. A larger time constant can more effectively suppress high-frequency interference, but it will significantly reduce the dynamic response speed of the system. On the contrary, a smaller time constant improves real-time performance, but due to insufficient attenuation of high-frequency components, unfiltered high-frequency harmonics and noise will enter the phase detection stage, thereby affecting estimation accuracy. Specifically, when the synchronization angle changes rapidly, the delay effect of the low-pass filter will cause the estimated phase angle to deviate from the true value. This deviation is not only related to the time constant of the low-pass filter, but also affected by the signal change rate. Therefore, when designing filter parameters, we must find a balance between real-time performance and filtering effect to meet the needs of practical applications.

In addition to the real-time performance, the low-pass filter parameters also directly affect the variance of the phase angle detection results. A large time constant can effectively smooth the random noise and reduce the detection variance, but it will also enlarge the delay effect. On the contrary, although a small time constant reduces the lag error, the detection variance may increase due to the high-frequency noise, which has not been significantly attenuated.

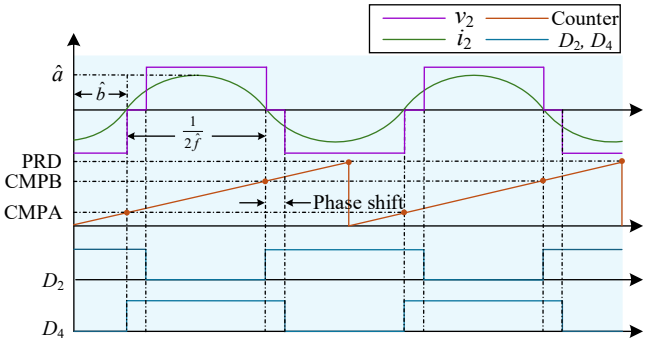

Fig. 3 Generation of the driving signals for D_2 and D_4. PRD is the period of the PWM counter, CMPA is the counter value to switch on D_4, and CMPB is the counter value to switch on D_2.

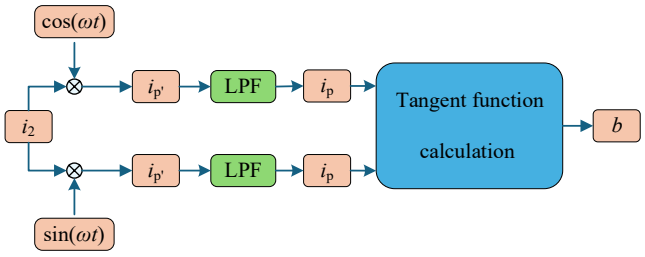

Fig. 4 Schematic diagram of active and reactive current decomposition for phase angle estimation.

Proposed frequency estimation method

Frequency estimation based on secondary bridge current

In the system operation process, optimal frequency estimation often encounters the challenge of local convergence. The primary cause of this issue lies in the non-convexity of the objective function during the optimization process. When iterative optimization algorithms are employed for frequency estimation, the algorithm could be trapped by local optima rather than converging to the global optimum. This phenomenon becomes particularly pronounced when the initial parameters are poorly selected.

To address this issue, during the initialization phase, the two lower switches of the active rectifier bridge can be shorted simultaneously to obtain more stable and reliable sampling data of the rectifier bridge input current. Based on these sampling data, the Gauss-Newton (GN) iterative algorithm can be applied to accurately estimate the frequency and initial phase angle of the rectifier bridge input current. The flowchart of the recursive algorithm is presented in Fig. 5.

It is necessary to estimate the amplitude a, the frequency f, and the initial phase b in real-time based on the sampled data $\{i_{2,\ell}^*\}_{\ell=1}^N$. Here, $(\cdot)^*$ denotes the sampled version of $(\cdot)$, and the subscript ℓ represents the sampling time index. The three parameters to be estimated are gathered in the vector $\theta = [a, f, b]^{\mathrm{T}}$, so the parameter estimation problem can be defined as follows:

$$\begin{aligned} \hat{\theta} &= \arg\min_{\theta} J(\theta) \\ J(\theta) &= \frac{1}{2}\sum_{\ell=1}^{N}\left(i_{2,\ell}^* - i_{2,\ell}\right)^2 \end{aligned} \tag{13}$$

The GN iterative algorithm can be employed to obtain a solution, in which the gradient vector and the Hessian matrix are defined as:

$$\begin{aligned}\nabla J(\theta) &= -\sum_{\ell=1}^{N}\phi_\ell(\theta)\left(i_{2,\ell}^{*}-i_{2,\ell}\right)\\ \nabla^2 J(\theta) &= \sum_{\ell=1}^{N}\phi_\ell(\theta)\phi_\ell^{T}(\theta)\end{aligned} \tag{14}$$

where,

$$\phi_\ell(\theta)=\left[\begin{array}{ccc}\frac{\partial i_2}{\partial a} & \frac{\partial i_2}{\partial f} & \frac{\partial i_2}{\partial b}\end{array}\right]^{\mathrm{T}}|_{t=t_\ell}=\left[\begin{array}{c}\sin(\omega t_\ell+b)\\ 2\pi t_\ell a\cos(\omega t_\ell+b)\\ a\cos(\omega t_\ell+b)\end{array}\right] \tag{15}$$

The cost function can be approximated by Taylor series expansion.

$$\begin{aligned}J(\theta)\approx J(\hat{\theta}_{k-1})+\nabla J(\hat{\theta}_{k-1})(\theta-\hat{\theta}_{k-1})+\\ \frac{1}{2}(\theta-\hat{\theta}_{k-1})^{\mathrm{T}}\left[\nabla^2 J(\hat{\theta}_{k-1})\right]^{-1}(\theta-\hat{\theta}_{k-1})\end{aligned} \tag{16}$$

where, $\hat{\theta}_{k-1}$ is an estimate of θ at the (k−1)th iteration. Consequently, by differentiating both sides of the equation with respect to θ, the solution that minimizes $J(\theta)$ can be obtained via an iterative procedure as follows:

$$\hat{\theta}_k=\hat{\theta}_{k-1}-\mu_k\Delta\hat{\theta}_k=\hat{\theta}_{k-1}-\mu_k\left[\nabla^2 J(\hat{\theta}_{k-1})\right]^{-1}\nabla J(\hat{\theta}_{k-1}) \tag{17}$$

where, μ_k is the scaling factor. It serves to prevent divergence caused by excessively large step sizes when the Hessian matrix is near singular and provides controllable convergence speed in highly nonlinear regions.

Frequency estimation based on the secondary bridge current

In multi-modal optimization problems, the characteristics of the loss function are usually manifested as the existence of a global optimal solution and multiple local optimal solutions. This complex structure can be described as: the objective function $J(\theta)$ has non convex characteristics within its domain, resulting in a multi-modal distribution of its solution space. Specifically, the global optimal solution θ^* is defined as satisfying $J(\theta^*)\leqslant J(\theta)$ for all points where $\theta\in\mathbb{D}$, where $\mathbb{D}$ represents the domain of the function. At the same time, there may exist multiple local optima $\{\theta_i\}_{i=1}^{N}$ within the same domain, which satisfy $J(\theta_i)\leqslant J(\theta)$, for any neighboring point $\theta\in\mathbb{N}(\theta_i)$, but do not guarantee reaching the global minimum. This multimodal nature poses a challenge to the optimization process, as algorithms may easily fall into local optima and fail to find the global optimum.

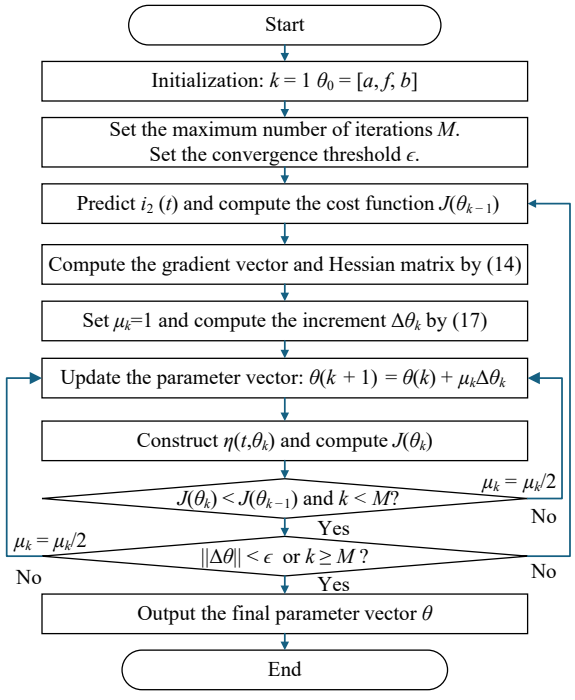

Fig. 5 Flowchart of parameter estimation for amplitude, frequency, and phase using the GN iterative algorithm.

The length of data N is one of the critical factors influencing the shape of the loss function curve. In practical applications, the size of N directly determines the richness of information available during parameter estimation, which in turn significantly impacts the smoothness of the loss function, the convergence rate, and the final optimization results. Figure 6 is generated through numerical simulation, showing the variation of the loss function $J(\theta)$ with frequency f under different data lengths N. The true parameters are: signal amplitude $a=2$, frequency $f=80$ kHz, initial phase $\varphi=-\pi$ rad, sampling rate 200 kS/s, with 30 dB Gaussian white noise added in the sampling process. In generating Fig. 6, it is assumed that a and φ are known while f is tried from a set of values in [60 100] kHz. It illustrates the impact of different data length N on the loss function curve and displays three curves corresponding to different values of N: 26, 76, and 152. When $N=26$, the loss function curve is relatively smooth, with a broad global minimum around 80 kHz. This indicates that for shorter data lengths, the loss function is less sensitive to variations in the input data, leading to a smoother optimization landscape. When $N=76$, the curve becomes more oscillatory, with several local minima emerging. This increased oscillation suggests that the loss function is more sensitive to the input data, making it harder for optimization algorithms to converge to the global minimum. When $N=152$, the curve exhibits even more pronounced oscillations, with multiple local minima becoming more distinct. The increasing complexity of the loss function curve demonstrates that longer data lengths introduce additional local optima, further complicating the optimization process.

These observations highlight the trade-off between data length and the complexity of the loss function. Shorter data lengths result in smoother loss functions but may fail to capture all relevant information. In contrast, longer data lengths provide more detailed information but introduce additional complexity in the form of multiple local optima. Careful consideration of data length is therefore essential to achieve an optimal balance between model precision and computational efficiency.

In addressing problems where the loss function exhibits multimodal characteristics, i.e., the presence of a global optimum and numerous local optima, a parameter estimation algorithm based on the GN iterative algorithm is proposed. The core idea of this algorithm is to dynamically adjust the data length N to enhance the convergence range and ultimately improve the accuracy of parameter estimation. The algorithm flowchart is shown in Fig. 7. Initially, the parameter vector θ to be estimated is initialized as the starting point for the first iteration, and the basic parameters of the signal, such as frequency and sampling period, are defined. At the same time, N is set to $N_{\min}$ as the initial data length. Throughout the optimization process, N is incrementally increased by a step size ΔN until it reaches $N_{\max}$. The GN iterative solution is performed using the initial parameter values of the current stage to obtain a new parameter estimate θ. To ensure that the optimization process effectively avoids being trapped in local optima, the parameter estimates obtained from the previous stage are used as the initial values for the next stage. In this way, the smaller data length N at the early stages allows the algorithm to search for possible solutions over a wider range, while the gradual increase in N enables the algorithm

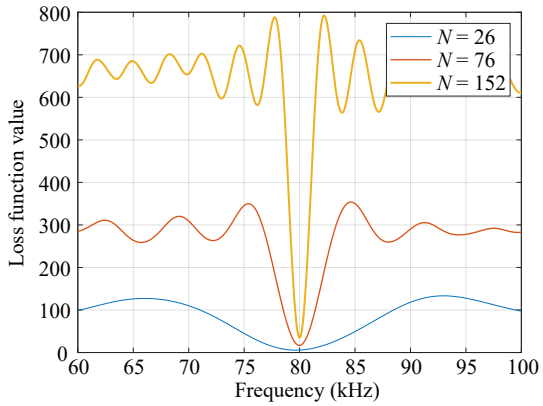

Fig. 6 Waveforms of the loss function under different data lengths.

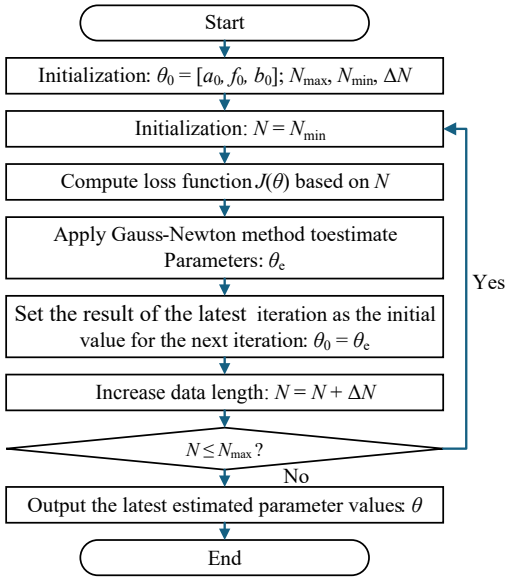

Fig. 7 Flowchart of iterative parameter estimation using the GN iterative algorithm with increasing data length.

to refine the parameter estimates on a more precise data basis, thereby achieving higher estimation accuracy. As shown in Fig. 8, when the data length N is set to the array [26, 72, 96, 152], for each value of N, 20 iterations of the GN iterative algorithm are performed to estimate the parameters θ of a sine curve with noise and third-harmonic distortion. This approach not only improves the selection of initial parameters but also effectively enhances the accuracy and stability of frequency estimation, thereby mitigating the impact of local convergence problems. The expression for this sine curve is as follows:

$$y = a \cdot \sin(2\pi\, ft + b) + 0.1\text{rand} \cdot \text{n}(t) + 0.3a \cdot \sin(6\pi\, ft) \tag{18}$$

where the amplitude $a = 2$, the frequency $f = 80$ kHz, and the initial phase angle $b = \pi$.

Figure 8 presents a comparison between the waveform estimated using the algorithm shown in Fig. 7 and the actual sine waveform with noise and harmonics. It also illustrates the gradual convergence of three parameters to their steady-state estimated values as the number of iterations increases from N_{min} to N_{max}, indicating that the fundamental component of the original waveform can be largely reconstructed. The variances between the three estimated parameters and their true values are presented in Table 1.

It can be observed that as the value of N gradually increases, the variances of the three estimated parameters all decrease, becoming increasingly closer to their true values.

In practical systems, measurement data are often affected by various noise sources, which can directly impact the performance and accuracy of parameter estimation algorithms. Specifically, when measurement data contain noise, the estimation algorithm may mistakenly treat the noise as part of the signal, causing the estimation results to deviate from the true values. To investigate this effect, we conducted Monte-Carlo simulation experiments by comparing the signal under different signal-to-noise ratio (SNR) conditions, analyzing the differences between the true parameters and the estimated parameters. The simulation results shown in Fig. 8 present the mean and standard deviation curves of the proposed algorithm's estimates for the amplitude, frequency, and period of a sine wave over an SNR range from 0 to 30 dB. Additionally, the figure includes a comparison between the waveform generated from the estimated parameters and the original sine wave. Simultaneously, Table 2 presents the specific values of the mean and standard deviation for the three estimated parameters.

Simulation verification

This section presents the validation of the proposed algorithm's effectiveness based on Simulink simulations. The parameters of the model used in the simulation are shown in Table 3. The low-pass filter for the PQ method is designed with a natural frequency of $\omega_n = 3{,}000$ rad/s, which corresponds to approximately 477 Hz. The filter is implemented as a second-order Butterworth filter, which ensures minimal distortion of the signal within the desired frequency range. The transfer function of the filter takes the form:

$$H(s) = \frac{9 \times 10^6}{s^2 + 4242.6s + 9 \times 10^6} \tag{19}$$

and its discrete-time version is given by:

$$Y(z) = \mathbf{C}_d(z\mathbf{I} - \mathbf{A}_d)^{-1}\mathbf{B}_d U(z) + \mathbf{D}_d U(z) \tag{20}$$

where:

$$\mathbf{A}_d = \begin{bmatrix} 0.9705 & 0.00485 \\ -43379 & 0.7831 \end{bmatrix}, \quad \mathbf{B}_d = \begin{bmatrix} 0.00485 \\ 43379 \end{bmatrix},$$
$$\mathbf{C}_d = \begin{bmatrix} 1 & 0 \end{bmatrix}, \quad \mathbf{D}_d = 0 \tag{21}$$

When the primary and secondary sides operate at inconsistent frequencies, directly estimating the initial phase angle after the rectifier input is in the steady state, without performing frequency estimation, can lead to the estimation of a time-varying initial phase angle as shown in Fig. 9. In Figs 10 and 11, with a frequency difference of 0.5% between the primary and secondary sides and $R_L = 6\,\Omega$, it can be observed that the resonant current waveform and the dc output waveform exhibit multiple spikes throughout the simulation time, such as those at time pointst_1, t_2, and t_3. These spikes occur when the estimated b on the secondary side umps from 2π to 0, generating false driving signals for the switches.

When estimating the frequency of the resonant current i_2, we account for the potential influence of harmonics. As shown in Fig. 12, the performance of the proposed frequency estimation algorithm is evaluated under different levels of harmonic distortion ($R_L = 20, 40, 60\,\Omega$). In this case, the frequency difference between the primary and secondary sides is 1.25%. It can be observed that the frequency estimation value (represented by the number of PWM counter cycles) converges from an initial value of 405 clock cycles (corresponding to a switching frequency of 50.625 kHz) to a nominal value of 400 clock cycles (corresponding to a design frequency of 50 kHz), indicating that the algorithm can still quickly track the true frequency under 1.25% frequency mismatch conditions.

The following section demonstrates the effect of PQ synchronization based on frequency estimation. As shown in Fig. 13, during the

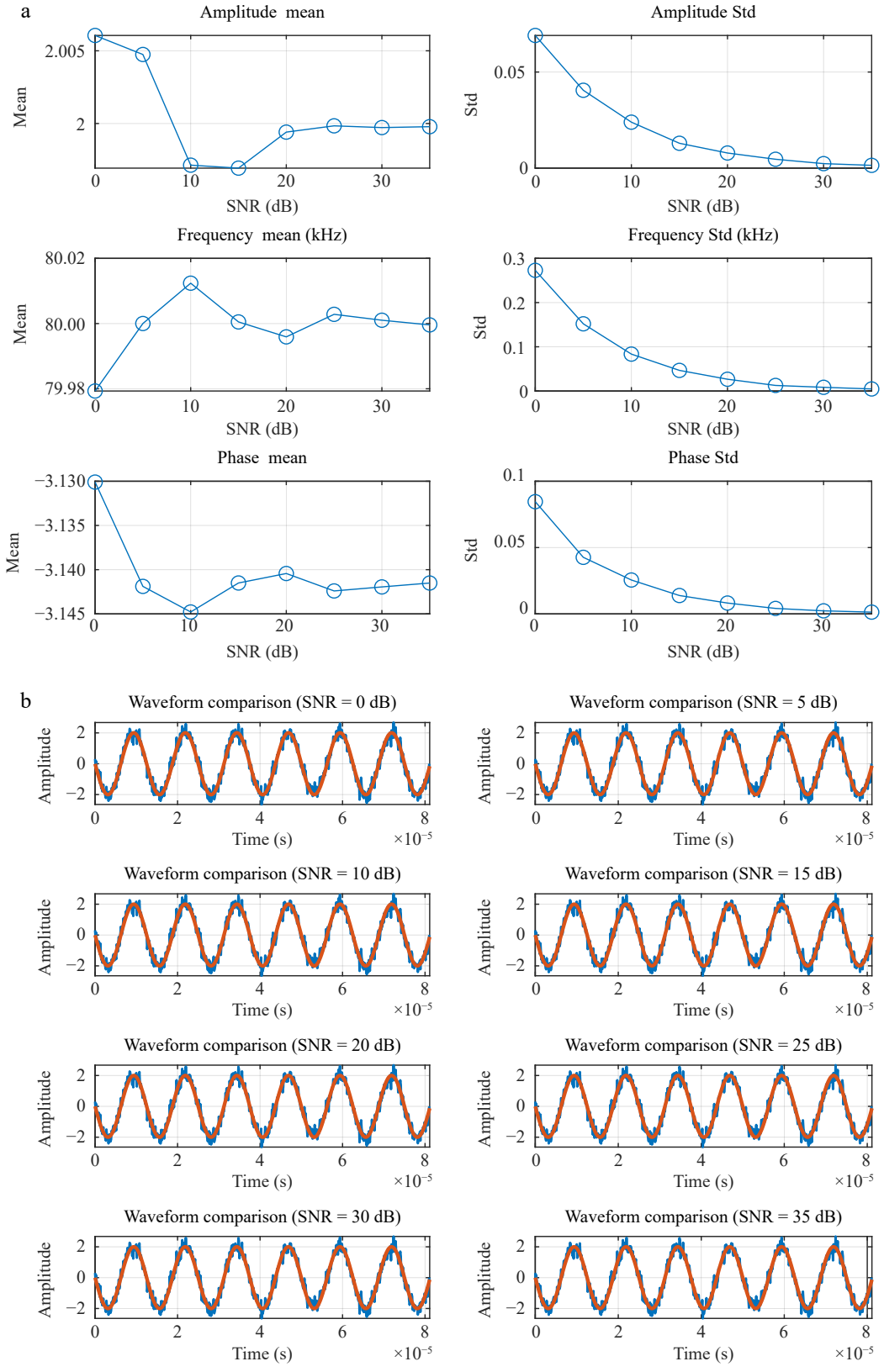

Fig. 8 Parameter estimates obtained under different SNRs. (a) Parameter estimates under different SNRs. (b) Comparion of the sampled noisy data and the estimated ones.

time interval t_0 to t_1, the two lower switches of the rectifier bridge are short-circuited simultaneously to obtain stable sampling data of the resonant current, and no parameter estimation is performed during this period. From t_1 to t_2, only precise frequency estimation is carried out to allow the frequency to converge stably to its actual value. In the subsequent phase starting from t_2, frequency estimation is stopped, and the initial phase angle is estimated instead to achieve synchronization. It can be seen that the situation where the initial phase angle estimate becomes time-varying due to the frequency difference no longer occurs. Additionally, the input current

Table 1. Variance and mean of estimated parameters for different data lengths.

N	Var ($\hat{a}$)	Var ($\hat{f}$)	Var ($\hat{b}$)
26	1.06×10^{-1}	1.25×10^{8}	2.96
72	6.20×10^{-4}	3.73×10^{3}	5.95×10^{-4}
96	4.66×10^{-4}	1.57×10^{3}	4.52×10^{-4}
152	2.88×10^{-4}	3.86×10^{2}	2.81×10^{-4}
N	Mean ($\hat{a}$)	Mean ($\hat{f}$)	Mean ($\hat{b}$)
26	0.377565	77.886872	−2.727483
72	1.997164	80.044921	−3.157094
96	1.998176	80.008205	−3.141797
152	2.005136	80.003889	−3.143130

Table 2. Estimated parameters.

SNR (dB)	Parameter	Ture value	Mean	Std
0	Amplitude	2	1.9937	8.13×10^{-2}
5	Amplitude	2	1.9940	3.86×10^{-2}
10	Amplitude	2	2.0012	2.62×10^{-2}
15	Amplitude	2	2.0022	1.54×10^{-2}
20	Amplitude	2	1.9994	7.29×10^{-3}
25	Amplitude	2	2.0006	4.73×10^{-3}
30	Amplitude	2	2.0001	2.36×10^{-3}
35	Amplitude	2	2.0002	1.29×10^{-3}
0	Frequency	80	80.022	267.36
5	Frequency	80	79.984	150.09
10	Frequency	80	80.014	82.733
15	Frequency	80	79.995	52.128
20	Frequency	80	79.999	26.779
25	Frequency	80	79.999	13.707
30	Frequency	80	80.000	8.5463
35	Frequency	80	80.000	4.4373
0	Phase	$-\pi$	−3.1518	7.95×10^{-2}
5	Phase	$-\pi$	−3.137	4.16×10^{-2}
10	Phase	$-\pi$	−3.1463	2.47×10^{-2}
15	Phase	$-\pi$	−3.1412	1.55×10^{-2}
20	Phase	$-\pi$	−3.1411	7.65×10^{-3}
25	Phase	$-\pi$	−3.1411	3.99×10^{-3}
30	Phase	$-\pi$	−3.1416	2.67×10^{-3}
35	Phase	$-\pi$	−3.1416	1.33×10^{-3}

Table 3. Main parameters of the LCC-LCC WPT system.

Symbol	Item	Value
C_p	Primary side compensation capacitor	80 nF
C_{f1}	Primary side parallel capacitor	120 nF
C_s	Secondary side compensation capacitor	80 nF
C_{f2}	Secondary side parallel capacitor	120 nF
C_f	Output filter capacitor	50 nF
L_p	Primary side coil self-inductance	200 μH
L_s	Secondary side coil self-inductance	200 μH
L_{f1}	Primary side compensation inductance	80 μH
L_{f2}	Secondary side compensation inductance	80 μH
M	Mutual inductance	55 μH
R_L	Load resistance	6 (default)/20/40/60 Ω
V_{dc}	DC power supply	200 V

of the rectifier bridge and the dc output no longer experience fluctuations caused by the loss of driving waveforms.

Experimental verification

In this section, the effectiveness of the proposed method is validated by experimental results. The prototype is shown in Fig. 14, which has a series-series compensation topology, with the main circuit parameters given in Table 4. The primary and secondary digital signal processors (DSPs) in the experiment are both TMS320f28377d, and the clock frequency of the ePWM module is 100 MHz. The resonant frequency is originally designed as 50 kHz, so the nominal counter period of the ePWM module is 2,000. The data used for frequency estimation is sampled at the rate of 200 kS/s.

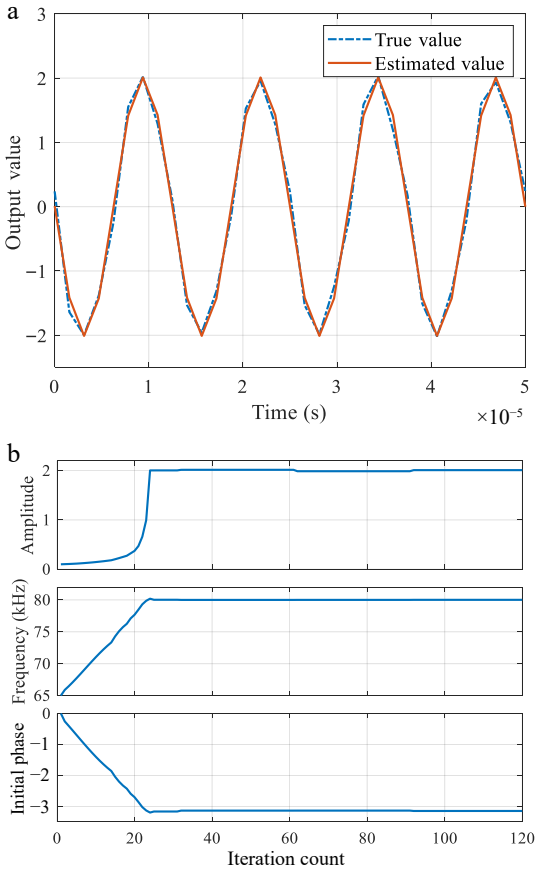

Fig. 9 Estimation results when the data length increases progressively. (a) Comparison of the sine waveform based on the final parameter estimates with the original waveform. (b) Variance and mean of estimated parameters.

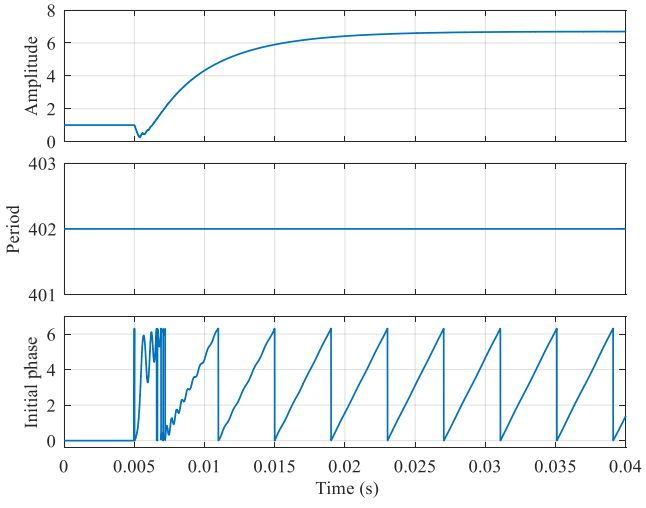

Fig. 10 Parameter estimates under primary-secondary frequency mismatch.

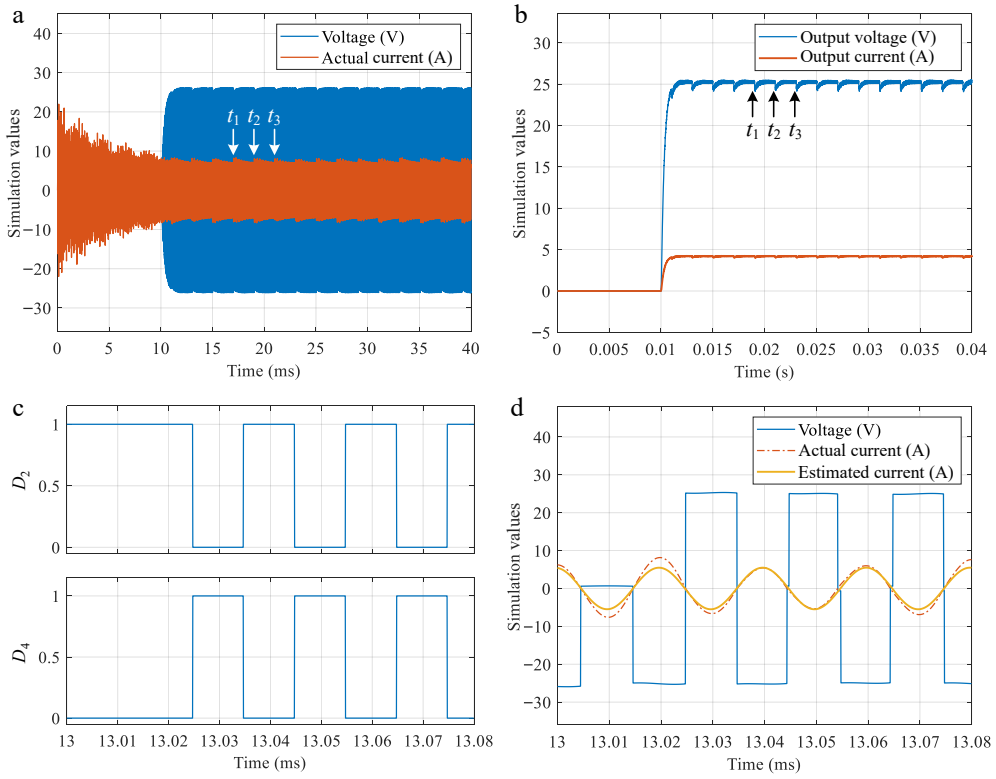

Fig. 11 Waveform under a primary-secondary frequency mismatch. (a) Waveform of voltage v_2 and current i_2. (b) Waveform of the output voltage and current of the load R_L. (c) Driving signals for D_2 and D_4. (d) Zooming-in waveform for v_2, i_2, and the estimated version of i_2.

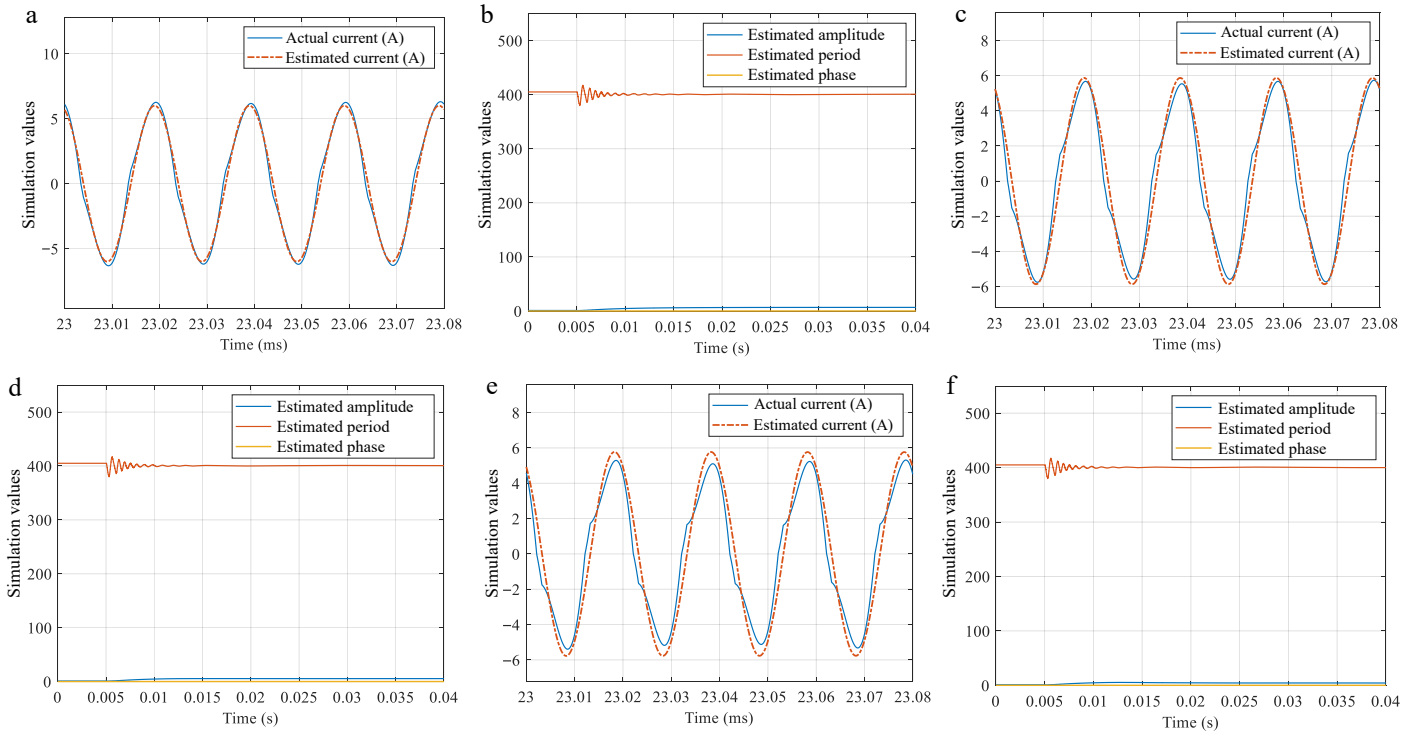

Fig. 12 Parameter estimates obtained under different levels of harmonic distortions. (a), (b): $R_L = 20\ \Omega$. (c), (d): $R_L = 40\ \Omega$. (e), (f): $R_L = 60\ \Omega$.

The frequency estimation procedure is slightly different to the one presented in the previous section. The main steps of the experiment are as follows:

- Switch off the four MOSFETs of the active rectifier to enable the diode bridge mode. When the system enters a stationary state, i_2 is sampled at the rate of 200 kHz to generate the data for frequency estimation.
- Estimate f_p based on the sampled data of i_2, which is accurate since i_2 will have the frequency of f_p once the system has reached a stationary state.

As another option in the first step of the above procedure, we can also specify an initial PWM frequency f_s for the secondary DSP, and then implement the PQ method to achieve active rectification. Theoretically, the initial phase estimated by PQ should be:

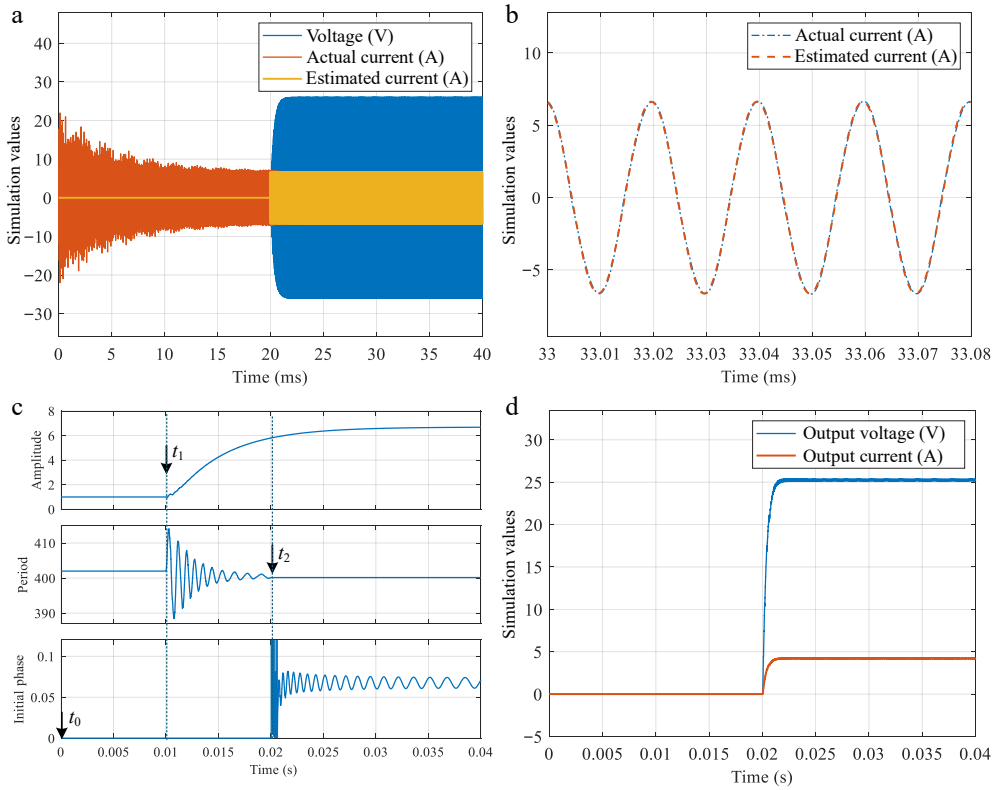

Fig. 13 Waveform of v_2 and i_2 using the estimated frequency. (a) Waveform of v_2, i_2, and the estimated i_2. (b) Zooming-in waveform of i_2, and the estimated i_2. (c) Parameter estimates. (d) Output voltage and current on R_L.

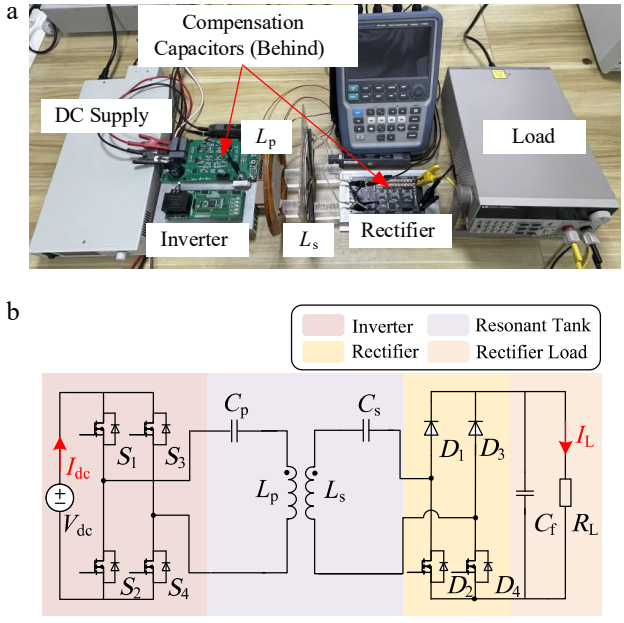

Fig. 14 SS compensated WPT system. (a) Prototype. (b) Circuit topology.

$$\hat{b} = 2\pi(f_s - f_p)t \tag{22}$$

which will be time varying if f_s is different from the primary PWM frequency f_p, or constant if $f_s = f_p$.

The oscilloscope data i_2 obtained in the diode bridge mode is given in Fig. 15, while the data sampled at the rate of 200 kS/s are presented in Fig. 16. Based on a set of 150 data points of i_2, the secondary frequency is estimated as:

Table 4. Main parameters of the SS WPT system.

Symbol	Item	Value
C_p	Primary side compensation capacitor	50.1 nF
C_s	Secondary side parallel capacitor	50.2 nF
C_f	Output filter capacitor	504.4 μF
L_p	Primary coil self-inductance	209.2 μH
L_s	Secondary coil self-inductance	204.4 μH
M	Mutual inductance	66.5 μH
R_L	Load resistance	10 Ω
V_{dc}	DC power supply	74 V

$$\hat{f}_s = 49.998\ \text{kHz} \tag{23}$$

Then, by using the estimated frequency as the basis to configure the PWM module of the secondary DSP, the waveform of v_1, i_1, v_2, and i_2 are shown in Fig. 17, while the estimated parameters are plotted in Fig. 18, where it can be seen that the estimated initial phase $\hat{b}$ becomes constant when the estimated frequency f_s in Eq. (20) is used to configure the PWM module.

By contrast, if the secondary frequency is not estimated, for example we just specify a coarse initial guess, e.g. $f_s = 50.5$ kHz, then the waveform of v_1, i_1, v_2, and i_2 take the form of Fig. 19. As shown therein, v_2 and i_2 do not perfectly aligned (their phase difference is not exactly π rad), this is due to the time varying initial phase, as shown in Fig. 20, which limits the real-time performance of synchronization.

Discussion

The method proposed in this article provides a data-based solution to accurately estimate the switching frequency of the primary side on the secondary side based on the sampled data of the rectifier input current, without the need for real-time wireless

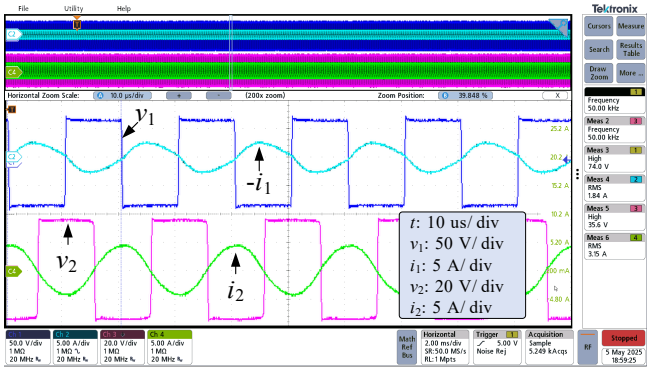

Fig. 15 Waveform of v_1, i_1, v_2, and i_2 in the diode bridge mode.

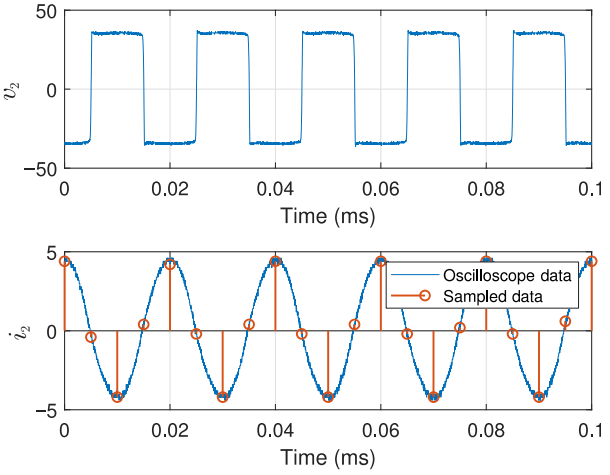

Fig. 16 Sampled data of i_2 in the diode bridge mode.

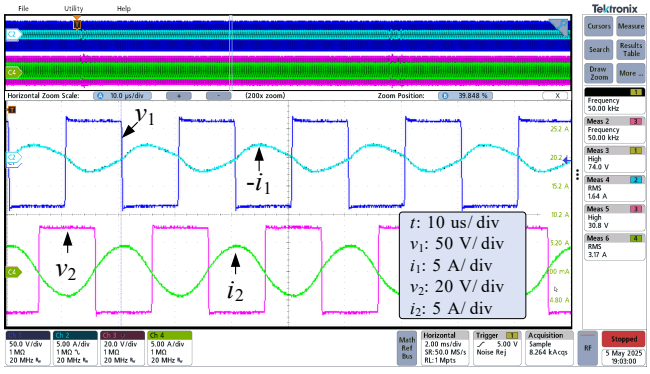

Fig. 17 Waveform of v_1, i_1, v_2, and i_2 in the active bridge mode, where the estimated secondary PWM frequency f_s = 49.998 kHz is used.

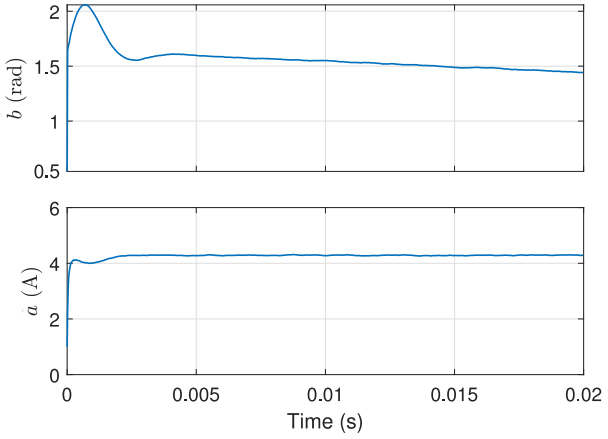

Fig. 18 Estimated parameters using the data presented in Fig. 17 (f_s = 49.998 kHz).

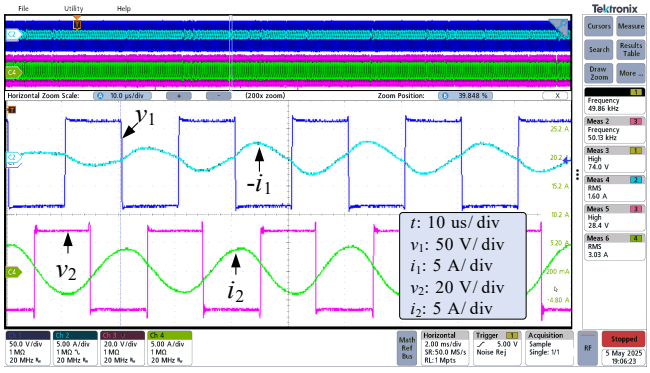

Fig. 19 Waveform of v_1, i_1, v_2, and i_2 in the active bridge mode with frequency mismatch (f_s = 50.5 kHz).

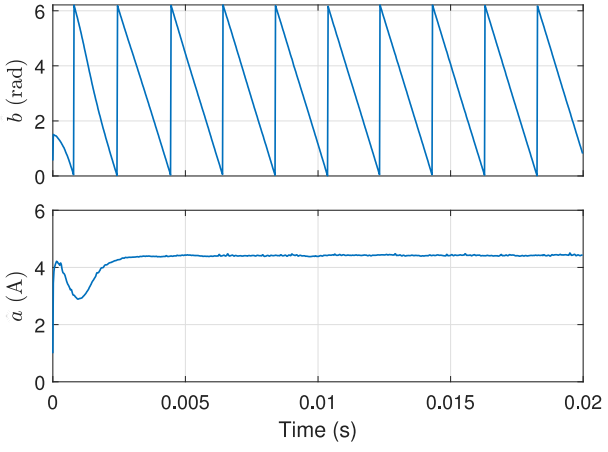

Fig. 20 Estimated parameters using the data presented in Fig. 19 (f_s = 50.5 kHz).

communication between the two sides. This method can be applied to conventional synchronization methods such as the PQ method to improve synchronization performance when the clock period of the primary-side controller is not equal to that of the secondary-side controller. The data-based mechanism has the merit of robustness to measurement noise, low hardware dependency, and high accuracy. These merit enables the proposed method to be easily integrated into the existing synchronization methods.

Conclusions

This article presents a resonant current-based frequency estimation method for phase synchronization in wireless power transfer systems. The method reduces real-time computational demands by accurately estimating frequency and phase parameters through the Gauss-Newton method. Key innovations include adaptive data window adjustment for improved convergence. Finally, the experimental results have validated the feasibility of the proposed method.

Author contributions

The authors confirm contributions to the paper as follows: conceptualization: Zhang Z; methodology: Zhang Z, Liu Y; writing: Qing X, Zhang Z, Chen Z; data curation: Qing X, Yang T; visualization:

Liu Y, Yang T; software and validation: Chen D, Chen F; funding acquisition: Chen Z. All authors reviewed the results and approved the final version of the manuscript.

Data availability

The datasets generated during and/or analyzed during the current study are available from the corresponding author on reasonable request.

Acknowledgments

This work was supported in part by the Natural Science Foundation of Chongqing (Grant No. CSTB2024NSCQ-MSX0086).

Conflict of interest

The authors declare that they have no conflict of interest.

Dates

Received 19 May 2025; Revised 21 June 2025; Accepted 7 July 2025; Published online 26 August 2025

References

1. Patil D, McDonough MK, Miller JM, Fahimi B, Balsara PT. 2018. Wireless power transfer for vehicular applications: overview and challenges. *IEEE Transactions on Transportation Electrification* 4(1):3–37
2. Song K, Ma B, Yang G, Jiang J, Wei R, et al. 2019. A rotation-lightweight wireless power transfer system for solar wing driving. *IEEE Transactions on Power Electronics* 34(9):8816–30
3. Qu J, He L, Tang N, Lee CK. 2020. Wireless power transfer using domino-resonator for 110-kV power grid online monitoring equipment. *IEEE Transactions on Power Electronics* 35(11):11380–90
4. Roy S, Azad ANMW, Baidya S, Alam MK, Khan F. 2022. Powering solutions for biomedical sensors and implants inside the human body: a comprehensive review on energy harvesting units, energy storage, and wireless power transfer techniques. *IEEE Transactions on Power Electronics* 37(10):12237–63
5. Yan Z, Zhang Y, Kan T, Lu F, Zhang K, et al. 2019. Frequency optimization of a loosely coupled underwater wireless power transfer system considering eddy current loss. *IEEE Transactions on Industrial Electronics* 66(5):3468–76
6. Yan Z, Song B, Zhang Y, Zhang K, Mao Z, et al. 2019. A rotation-free wireless power transfer system with stable output power and efficiency for autonomous underwater vehicles. *IEEE Transactions on Power Electronics* 34(5):4005–8
7. Zhou J, Zhang B, Xiao W, Qiu D, Chen Y. 2019. Nonlinear parity-time-symmetric model for constant efficiency wireless power transfer: application to a drone-in-flight wireless charging platform. *IEEE Transactions on Industrial Electronics* 66(5):4097–107
8. Zhao S, Tang C, Chen F, Zhao D, Deng P, et al. 2023. Modeling and control of the WPT system subject to input nonlinearity and communication delay. *IEEE Transactions on Power Electronics* 38(11):14776–87
9. Liu X, Jin N, Ma D, Yang X. 2018. A simple and effective synchronization technique for wireless power transfer system. In *2018 IEEE Wireless Power Transfer Conference (WPTC), Montreal, QC, Canada, 2018*. pp. 1–4 doi: 10.1109/WPT.2018.8639242
10. Tan T, Chen K, Jiang Y, Lin Q, Yuan L, et al. 2020. A bidirectional wireless power transfer system control strategy independent of real-time wireless communication. *IEEE Transactions on Industry Applications* 56(2):1587–98
11. Thrimawithana DJ, Madawala UK, Neath M. 2013. A synchronization technique for bidirectional IPT systems. *IEEE Transactions on Industrial Electronics* 60(1):301–9
12. Mai R, Liu Y, Li Y, Yue P, Cao G, et al. 2018. An active-rectifier-based maximum efficiency tracking method using an additional measurement coil for wireless power transfer. *IEEE Transactions on Power Electronics* 33(1):716–28
13. Zhang Y, Chen S, Li X, Tang Y. 2021. Dual-side phase-shift control of wireless power transfer implemented on primary side based on driving windings. *IEEE Transactions on Industrial Electronics* 68(9):8999–9002
14. Zhang Y, Li X, Chen S, Tang Y. 2022. Soft switching for strongly coupled wireless power transfer system with 90° dual-side phase shift. *IEEE Transactions on Industrial Electronics* 69(1):282–92
15. Zheng K, Ren J, Zhong W. 2025. A soft-switching secondary-side control method without AC current detection for wireless power transfer systems. *IEEE Transactions on Power Electronics* 40(2):3785–97
16. Gati E, Kampiisis G, Manias S. 2017. Variable frequency controller for inductive power transfer in dynamic conditions. *IEEE Transactions on Power Electronics* 32(2):1684–96
17. Tang Y, Chen Y, Madawala UK, Thrimawithana DJ, Ma H. 2018. A new controller for bidirectional wireless power transfer systems. *IEEE Transactions on Power Electronics* 33(10):9076–87
18. Li M, Deng J, Chen D, Wang W, Li Y, et al. 2023. A minimum ZVS current control strategy of semi bridgeless active rectifier for wide operation range based on LCC-S compensated WPT system. *IEEE Transactions on Industry Applications* 59(3):3481–92
19. Ann S, Lee BK. 2021. Analysis of impedance tuning control and synchronous switching technique for a semibridgeless active rectifier in inductive power transfer systems for electric vehicles. *IEEE Transactions on Power Electronics* 36(8):8786–98
20. Zhang X, Cai T, Duan S, Feng H, Hu H, et al. 2019. A control strategy for efficiency optimization and wide ZVS operation range in bidirectional inductive power transfer system. *IEEE Transactions on Industrial Electronics* 66(8):5958–69
21. Hu Y, Han W, Zhang B, Hu W. 2025. An active-rectifier wireless motor system with dual-side phase shift control for phase synchronization and efficiency optimization. *IEEE Transactions on Power Electronics* 40(2):3798–809
22. Cochran S, Costinett D. 2018. Frequency synchronization and control for a 6.78 MHz WPT active rectifier. In *2018 IEEE 19th Workshop on Control and Modeling for Power Electronics (COMPEL), Padua, Italy, 2018*. pp. 1–7 doi: 10.1109/COMPEL.2018.8459998
23. Fu M, Yin H, Zhu X, Ma C. 2015. Analysis and tracking of optimal load in wireless power transfer systems. *IEEE Transactions on Power Electronics* 30(7):3952–63
24. Mostafa TM, Bui D, Muharam A, Hu AP, Hattori R. 2020. Load effect analysis and maximum power transfer tracking of CPT system. *IEEE Transactions on Circuits and Systems I: Regular Papers* 67(8):2836–48
25. Liu F, Li K, Chen K, Zhao Z. 2020. A phase synchronization technique based on perturbation and observation for bidirectional wireless power transfer system. *IEEE Journal of Emerging and Selected Topics in Power Electronics* 8(2):1287–97